Nanoscale

ROYAL SOCIETY OF CHEMISTRY

PAPER

View Article Online
View Journal | View Issue

Cite this: *Nanoscale*, 2023, **15**, 16314

A cascade nanoplatform for the regulation of the tumor microenvironment and combined cancer therapy†

Xiaochun Hu,‡[a,b] Wenrong Zhao,‡[a] Ruihao Li,[a] Keke Chai,[a] Fangjian Shang,[c] Shuo Shi *[a] and Chunyan Dong *[a]

Recently, disulfiram (DSF), an anti-alcoholism drug, has attracted increasing biomedical interest due to its anticancer effects. However, the anticancer activity of DSF is Cu(II)-dependent and it is extremely unstable, which severely hinders its clinical translation. Herein, we report the fabrication of a multifunctional nanoplatform (MCDGF) that can improve the stability of diethyldithiocarbamate (DTC), a main metabolite of DSF, by modifying the aryl boronic ester group to form a prodrug (DQ), and also realize the *in situ* generation of $Cu(DTC)_2$, which relies on a cascade reaction. The delivered Cu/DQ induces immunogenic cell death (ICD) and powerfully enhances immune responses of cytotoxic T lymphocytes (CTLs) and the infiltration of dendritic cells as well as T cells. Furthermore, the grafted glucose oxidase (GOx) decomposes glucose, thus "starving" the cancer cells and providing H_2O_2 for the production of $Cu(DTC)_2$. More importantly, H_2O_2 significantly promotes the polarization of macrophages to the anti-tumor subtype. The nano-carrier "mesoporous polydopamine (MPDA)" also displays a good photothermal therapeutic effect. The nanoplatform-integrated chemotherapy, starvation therapy, photothermal therapy, and immunotherapy synergistically stimulated CTL activation and M1 macrophage polarization. Taken together, the as-prepared nanoplatform could regulate the tumor immune microenvironment and eliminate cancer with combined cancer therapy, which will offer a promising strategy for cancer treatment and promote the clinical application of DSF in breast cancer.

Received 2nd July 2023,
Accepted 13th September 2023

DOI: 10.1039/d3nr03199c

rsc.li/nanoscale

1. Introduction

In 2020, female breast cancer surpassed lung cancer as the most commonly diagnosed cancer, with an estimated 2.3 million new cases,[1] and triple-negative breast cancer (TNBC) accounted for 15–20% of breast cancer, which was characterized by its being more prone to early recurrence and its aggressive behavior.[2,3] For TNBC treatment, chemotherapy is still the most efficient method on the account of the lack of specific therapeutic targets. However, the drug resistance and side-effects of traditional chemotherapeutic drugs have severely limited the prognosis of TNBC. Therefore, it is of great significance to develop new therapeutic drugs and new combined therapy.[4] With increasing reports on the novel functions of clinical drugs, new applications of old drugs have gradually become an attractive trend in drug development owing to their lower cost, shorter periods, and higher success rates.[5] Typically, disulfiram, artemisinin and aspirin have presented positive results in cancer therapy.[6,7]

As a classical drug for alcoholism, DSF has obtained approval from the Food and Drug Administration (FDA) and has been employed in America for several decades owing to its good safety and negligible side effects.[8] For the past few years, the excellent anticancer activity of DSF *in vitro* and *in vivo* has attracted widespread attention.[9] Diethyldithiocarbamate (DTC) is a main metabolite of DSF, which tends to chelate Cu(II) to give $Cu(DTC)_2$. In 2017, Skrott *et al.* confirmed that the formation of $Cu(DTC)_2$ was the key active ingredient, which would bind nuclear protein localization-4 (NPL4) and induce its aggregation, blocking out the vital p97-NPL4-UFD1 pathway and leading to tumor cell death.[10] Recently, a few studies have demonstrated that $Cu(DTC)_2$ could trigger immunogenic cell death (ICD) in tumor cells,[11,12] producing damage-associated pattern signaling, including the secretion of adenosine tripho-

[a]*Department of Comprehensive Cancer Therapy, Shanghai East Hospital, School of Medicine, Shanghai Key Laboratory of Chemical Assessment and Sustainability, School of Chemical Science and Engineering, Tongji University, Shanghai 200092, China. E-mail: shishuo@tongji.edu.cn, cy_dong@tongji.edu.cn*
[b]*School of Medicine, Shanghai University, Shanghai 200444, China*
[c]*College of Aeronautical Engineering, Binzhou University, Binzhou 256603, China*
†Electronic supplementary information (ESI) available. See DOI: https://doi.org/10.1039/d3nr03199c
‡These authors contributed equally to this work.

sphate (ATP), release of high-mobility group box 1 (HMGB1) and translocation of calreticulin (CRT). ICD is a cell death modality that was developed as an immunostimulatory initiator to induce systemic anti-tumor immunity and suppress the growth of tumors.[13,14] Meanwhile, as far as we know, the work of DSF in inducing the ICD of TNBC cells has not been reported. Therefore, it is of great significance to carry out research on DSF in the treatment of triple-negative breast cancer by triggering chemotherapy and immunotherapy. Nevertheless, DSF is highly unstable in the bloodstream and has a short plasma half-life (4 min), and $Cu(DTC)_2$ also presents obvious toxicity for normal tissues, which greatly limits the clinical translation.[15] Thus, improving the stability of DSF and generating $Cu(DTC)_2$ *in situ* are of great significance in promoting the clinical application of disulfiram.

The construction of prodrugs was regarded as a feasible strategy to overcome the instability of chemotherapeutic drugs.[16] Prodrugs could transform the activity component by stimulating the tumor microenvironment (TME), and the fabrication of prodrugs could reduce the toxicity toward normal tissue and extend the circulation time.[17] Usually, the activation of the prodrug is achieved by modification with special functional groups that are responsive to triggers in the tumor.[18,19] For instance, aryl boronic esters could be applied as H_2O_2-responsive groups, and the B–C bond would be cleaved under H_2O_2 stress.[20]

Nanoparticles (NPs) with excellent properties such as targeted delivery, response-specific release, and the generation of anti-cancer drugs *in situ* have been widely applied to load chemotherapeutic agents.[21–23] Among the various nanomaterials that have been reported, as a mussel-inspired material, polydopamine has attracted great attention from researchers owing to its biocompatibility, easy surface modification and outstanding photothermal-conversion ability.[24] In addition, mesoporous polydopamine (MPDA) has been constructed, which features abundant mesoporous structures for use as an efficient drug carrier.[25,26]

Herein, a mesoporous polydopamine-based nanoplatform (MPDA-Cu/DQ-GOx-FA/PEG, MCDGF) was fabricated, which can improve the stability of DSF by modifying the aryl boronic ester group to form a prodrug (DQ), and also realize *in situ* $Cu(DTC)_2$ generation, relying on a cascade reaction between glucose oxidase (GOx) and DQ (Scheme 1). GOx was grafted onto the surface of the nanoplatform *via* a convenient Schiff/Michael reaction, which is known for catalyzing glucose to gluconic acid and H_2O_2 and triggering starvation therapy.[27,28] More importantly, H_2O_2 can reorient the pro-tumor M2 tumor-associated macrophages (TAMs) to the anti-tumor M1 TAMs.[29–31] Folic acid (FA) receptors were overexpressed on TNBC cells, to improve the active target delivery, biocompatibility, and water solubility of the nanoplatform; FA/PEG was modified on the surface of the nanoplatform. This novel nanoplatform, to improve the curability of TNBC, possesses the following advantages. (a) The nanoplatform could accumulate in the tumor by active target-delivery and release DQ triggered by laser irradiation, the glucose in the tumor was catalyzed by

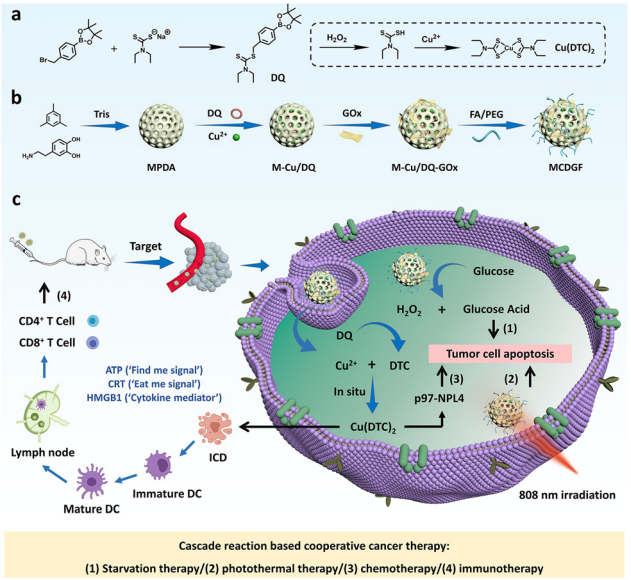

Scheme 1 (a) The synthetic route of DQ and the generation of $Cu(DTC)_2$ in the presence of H_2O_2. (b) The synthetic route of MCDGF. (c) Schematic illustration of the application of MCDGF for *in situ* generation of $Cu(DTC)_2$ and cooperative cancer therapy.

GOx to gluconic acid and H_2O_2, and the starvation therapy was activated, and then DQ would be transformed into DTC by reacting with H_2O_2 and chelate with co-released Cu(II) to produce $Cu(DTC)_2$ *in situ*. (b) The produced $Cu(DTC)_2$ could induce tumor cell apoptosis and lead to ICD, which is beneficial for enhancing the infiltration of cytotoxic T lymphocytes (CTLs), and H_2O_2 could polarize MDSCs toward the M1 phenotype to reduce the tumor burden. (c) Under 808 nm laser irradiation, MPDA eradicates cancer cells efficiently by thermal ablation, which would further induce breast cancer cell death. Notably, our study presents a cascade reaction-based harmonious integration of chemotherapy, photothermal therapy (PTT), starvation therapy and immunotherapy in one nanoplatform to realize a safe and effective treatment for TNBC.

2. Results and discussion

2.1. Preparation and characterizations of the MCDGF

Initially, the prodrug (DQ) with the responsiveness to H_2O_2 was synthesized successfully according to the reported method[15] and characterized by NMR and ESI-MS (Fig. S1–S3†). MPDA was prepared[32] (Fig. 1a and c), and Cu(II) could be doped in MPDA by Cu–N coordination interactions,[33] and DQ would be encapsulated in MPDA *via* intermolecular forces.[34] Through the Michael addition or Schiff base reaction, the catechol groups on the surface of MPDA could react with amines or thiols under alkaline conditions.[35] As a result, both GOx and polyethylene glycol (PEG, terminated with amino and FA) were modified on the surface of M-Cu/DQ to obtain a multifunctional nanoplatform, MCDGF. As shown in Fig. 1b and d,

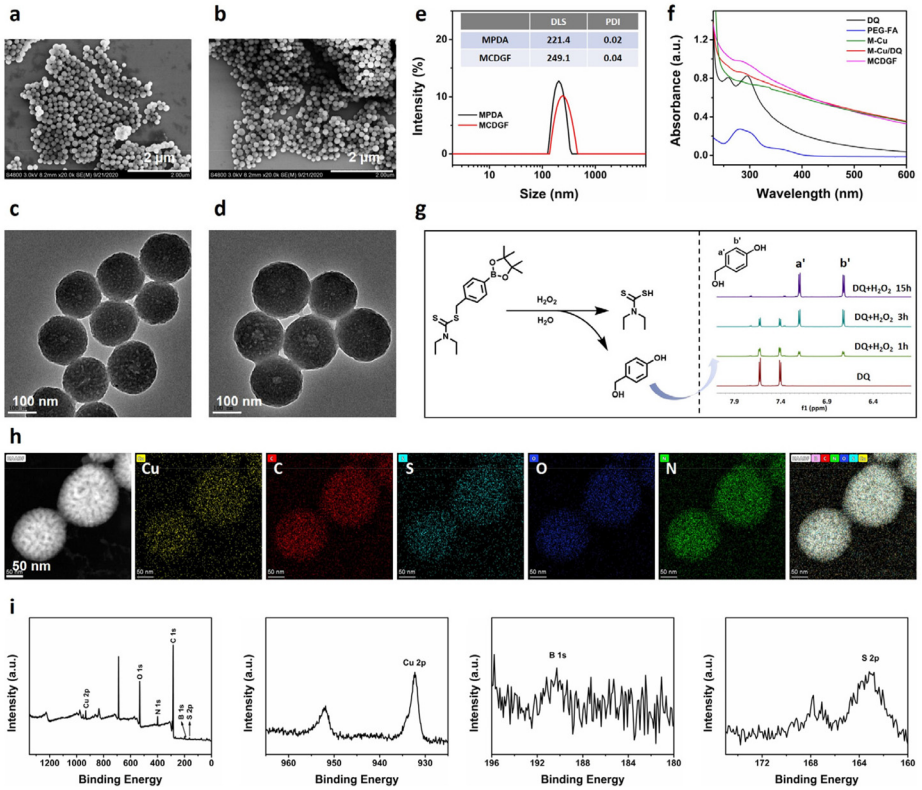

Fig. 1 SEM images of (a) MPDA and (b) MCDGF. TEM images of (c) MPDA and (d) MCDGF. (e) DLS and PDI of nanoparticles in water. (f) UV-Vis absorption spectra of different nanoparticles, free DQ and free FA/PEG. (g) ^{1}H NMR spectral changes of DQ in the presence of H_2O_2. (h) Elemental mapping of MCDGF. (i) XPS results of MCDGF.

the mono-dispersity of MCDGF was well maintained after GOx and FA/PEG modification, while the low polydispersity index (PDI) parameter also proved the good dispersion property of MCDGF (Fig. 1e). According to the Fourier transform infrared (FTIR) results, the characteristic peak at 2885 cm^{-1} of MCDGF was attributed to PEG (Fig. S4†). Based on the bicinchoninic acid (BCA) protein assay kit,[35] the loading capacity of GOx was about 8.1%. The loading capacity of FA was calculated to be 3.4% based on the standard calibration (Fig. S5†). MPDA presented an average hydrodynamic diameter of about 221.4 nm, while the size of MCDGF increased to 249.1 nm because of the grafting of FA/PEG and GOx (Fig. 1e). The UV-vis absorption spectra of M-Cu/DQ showed a characteristic peak of DQ at 286 nm. The characteristic peak of DQ shifted from 294 nm to 286 nm after loading into MPDA on account of the hydrogen bond between DQ and MPDA (Fig. 1f and S6a†). The elemental mapping images (Fig. 1h and S6b†) indicated that the elements of C, N, O, S, B and Cu were uniformly distributed in MCDGF. X-ray photoelectron spectroscopy (XPS) results also showed the existence of objective elements (C, N, O, S, B and Cu) on MCDGF (Fig. 1i and S6c†). According to the results from inductively coupled plasma optical emission spectroscopy (ICP-OES), the loading capacities of Cu(II) and DQ were about 4.7% and 7.9%. Taken together, the above results demonstrated the successful synthesis of MCDGF nanoparticles.

2.2. H_2O_2-responsiveness of the nanoplatform

First, the H_2O_2-responsiveness of DQ was verified by ^{1}H NMR (Fig. 1g and S7†). The ^{1}H NMR spectra of DQ in the solution of DMSO-d_6/D_2O (v/v, 9 : 1) with H_2O_2 were obtained at the determined times. With time, the characteristic peaks at 6.7 and 7.2 ppm belonging to 4-hydroxybenzyl alcohol, appeared and became elevated, which revealed that DTC could be released from DQ in the presence of H_2O_2. For the control, little cleavage product (4-hydroxybenzyl alcohol) of DQ was detected in the absence of H_2O_2 after 15 h, demonstrating no release of DTC without H_2O_2 (Fig. S7†).

The production of H_2O_2 and gluconic acid and the consumption of O_2 by MCDGF were elevated. The concentration of dissolved oxygen in the reaction system was monitored by a dissolved oxygen meter. Upon the addition of MCDGF into the solution of glucose (100 mM or 200 mM), the concentration of oxygen in the reaction system reduced rapidly due to the consumption of dissolved oxygen for glucose oxidation, which was catalyzed by the loaded GOx (Fig. 2a). In addition, the hydrogen peroxide detection kit was used to detect the generated H_2O_2, which was a reaction product from the catalysis of glucose by MCDGF, and the results revealed abundant H_2O_2 generated during the glucose oxidation reaction (Fig. 2b). Next, gluconic acid, another product of the reaction, was monitored by a gluconic acid-specific colorimetric assay. Specifically,

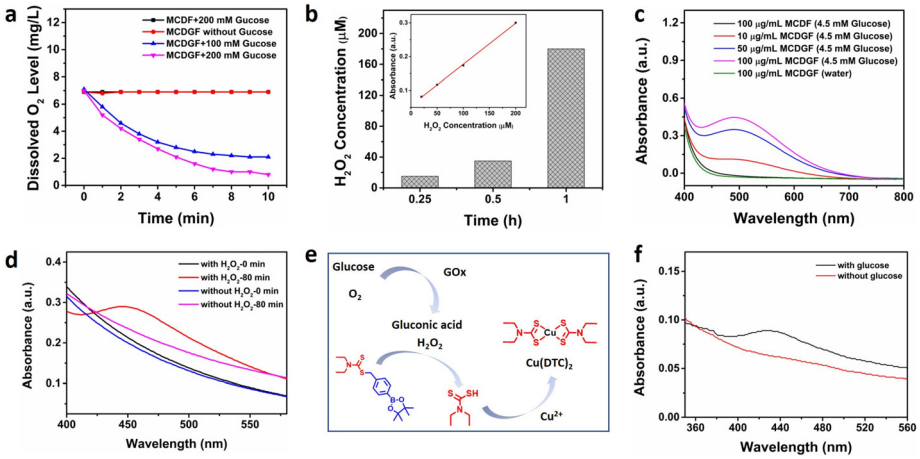

Fig. 2 (a) Dissolved O_2 levels of the MCDGF dispersion after incubation with glucose. (b) The generated H_2O_2 concentration of the MCDGF dispersion containing glucose (4.5 mM) with 0.25, 0.5 and 1 h incubation; inset: the standard curve of GOx. (c) The catalytic ability of MCDGF determined by UV-vis spectroscopy. (d) The absorption spectra of various DQ and $CuCl_2$ mixture solutions in the presence or absence of H_2O_2. (e) The formation of $Cu(DTC)_2$ based on the cascade reaction. (f) The supernatant absorbance spectra of the dispersion containing MCDGF after immersing in SBF in the presence or absence of glucose (4.5 mM) for 24 h.

MCDGF was incubated with 4.5 mM glucose solution for 30 min, and the supernatant was retained. After adding hydroxylamine and Fe(III) to the above supernatant, the solution turned red and the characteristic absorption peak at 505 nm was elevated with the increasing concentrations of MCDGF (Fig. 2c and S8†), which verified the production of gluconic acid and confirmed the catalytic activity of MCDGF.

To further investigate the H_2O_2-responsive release of DTC and the formation of $Cu(DTC)_2$ in the presence of Cu(II), the absorption spectra were obtained to monitor the reaction process. As shown in Fig. 2d, a new characteristic absorption peak of $Cu(DTC)_2$ at 440 nm was observed, demonstrating the chelation between DTC and Cu(II). Sequentially, the $Cu(DTC)_2$ generation behavior of MCDGF in the presence of glucose was verified *in vitro*. As designed, the reaction was initially cascaded by GOx, which catalyzed the glucose in the tumor to generate abundant H_2O_2. As the reactant for the subsequent catalytic reaction, the obtained H_2O_2 would react with DQ to liberate DTC, generating $Cu(DTC)_2$ to effectively induce cancer cell death (Fig. 2e). As shown in Fig. 2f, after MCDGF was incubated in simulated body fluid (SBF) with 4.5 mM glucose, there was an obvious absorption peak at 440 nm, demonstrating the formation of $Cu(DTC)_2$. In contrast, in the absence of glucose, the intensity of $Cu(DTC)_2$ characteristic peak was weak.

2.3. Photothermal performance of the nanoplatform and DQ release *in vitro*

MCDGF showed a distinct absorption in the NIR region, which was beneficial to the photothermal conversion. In particular, the absorption intensity of MCDGF at 808 nm increased linearly with the concentration, indicating the fine dispersity of NPs in aqueous solution (Fig. S9a†). In addition, MCDGF could also be well dispersed in PBS, SBF, DMEM and DMEM (FBS) solutions without obvious aggregation overnight (Fig. S9b†). To explore the applicability of prefabricated MCDGF, the photothermal properties of MCDGF with gradient concentrations were monitored by an infrared thermal camera under 808 nm laser irradiation for 5 min. There was no obvious elevation of temperature for H_2O upon irradiation. Expectedly, MCDGF with varying concentrations (25, 50, 100, 200 μg mL^{-1}) revealed a significant increase, demonstrating good photothermal conversion efficacy (Fig. 3a). MCDGF dispersion also presented a power-dependent photothermal conversion efficacy (Fig. 3b).

Importantly, MCDGF presented outstanding stability and reproducibility, proved by its photothermal performance remaining unchanged after five repeated laser on/off cycles (Fig. 3c), and the photothermal conversion efficiency (η) was calculated to be 21% (Fig. 3d). In addition, under 808 nm laser irradiation, MCDGF presented the potential to realize photothermal imaging *in vivo* (Fig. 3e). The remarkable PTT property of MCDGF supported further evaluation of its photothermal cytotoxicity *in vitro* and *in vivo*.

With 808 nm laser irradiation, the cumulative release of DQ was higher than that without irradiation (Fig. 3f). For example, the release percentage reached 46.9% as compared with 20.3% for the control without irradiation at 36 h intervals. The binding energy of DQ with MPDA was calculated to be −9.9 kcal mol^{-1} based on the DFT method (Gaussian 09, b3lyp/6-31 g*, PCM) (Fig. S10†), which revealed that DQ was loaded on the MPDA nanoplatform *via* intermolecular forces, hydrogen bonding and π–π stacking.[36] The faster release of DQ from MCDGF under laser irradiation was attributed to local hyperthermia weakening the interaction between DQ and MPDA.[37] There was a similar photothermal responsive release behaviour for Cu(II). As a result, MCDGF presented good stability during the delivery processes, and DQ and Cu(II) were

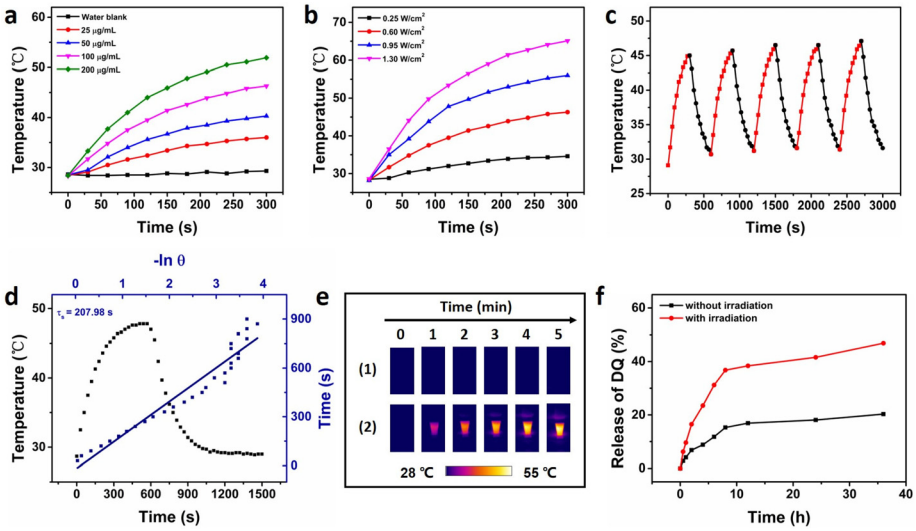

Fig. 3 (a) Temperature elevation of the MCDGF with different concentrations (0.6 W cm^{-2}). (b) The induced temperature of MCDGF (100 μg mL^{-1}) within 5 min under irradiation by an 808 nm laser with varied power densities. (c) Temperature change curves of MCDGF (100 μg mL^{-1}, 0.6 W cm^{-2}) over five repeated laser on/off cycles. (d) Calculated photothermal-conversion efficiency of MCDGF (100 μg mL^{-1}, 0.6 W cm^{-2}) at 808 nm. Blueline: the corresponding linear fitting curve between the plot of cooling time data and $-\ln\theta$. (e) Representative photothermal images of MCDGF dispersion (0.6 W cm^{-2}, 5 min). (1) Water, (2) 200 μg mL^{-1} MCDGF dispersion. (f) DQ release behavior from MCDGF with or without irradiation.

released when 808 nm laser irradiation was carried out (Fig. S11a–c†). Meanwhile, the activity of GOx would not be influenced by laser irradiation, elevated temperature (42 °C) or the existence of $Cu(DTC)_2$ (Fig. S11d†).

2.4. Cytotoxicity assessment and cellular uptake of the nanoplatform

We determined the antitumor activity of each treatment group *in vitro*. As shown in Fig. S12a,† DQ exhibited great toxicity to 4T1 cells when Cu(II) and H_2O_2 were used concomitantly, and was non-toxic without Cu(II) (Fig. S12b†). This was because the initial copper concentration in 4T1 cells was very low and the generated $Cu(DTC)_2$ would be insufficient to induce apoptosis. The drug-free M-PEG nanoparticles exhibited little effect in 4T1 cell growth as expected, which verified the safety of the nanocarrier. When irradiated by an 808 nm laser (1.5 W cm^{-2}, 10 min), the nanoparticles exerted a significant antitumor effect. The toxicity of nanoparticles loaded with GOx or Cu/DQ to 4T1 cells was relatively weak, and it gradually appeared only when the concentration exceeded 20 μg mL^{-1}. Excitingly, the combination therapy (MCDG + PTT or MCDGF + PTT) demonstrated an incomparable ability in the growth inhibition of 4T1 cells (Fig. 4a and S12d†).

The AM/PI co-staining experiment was carried out to further evaluate the synergistic therapy, in which red fluorescence indicated dead cells and green fluorescence indicated living cells. The green fluorescence in group MCDGF + PTT was negligible, indicating that almost all the cells were dead (Fig. S12c†). The results were consistent with the cytotoxicity assessment by the CCK8 method. Next, the uptake of MCDG and MCDGF by 4T1 cells was compared. Images were acquired by confocal laser scanning microscopy (CLSM) (Fig. 4b). Ce6-labeled MCDGF presented red fluorescence in the cytoplasm of 4T1 cells after incubation for 4 h, while only weak red fluorescence was observed if treated with MCDG (without conjugation of FA). Furthermore, the targeting efficiency of MCDGF was evaluated quantitatively by flow cytometry analysis. The phagocytosis of nanoparticles by 4T1 cells increased over time and MCDGF conjugated with FA were taken up more efficiently (Fig. 4c and S12c†). Both CLSM images and flow cytometry results revealed that MCDGF could be internalized efficiently by 4T1 cells in a folate receptor-specific manner.

Afterwards, the efficacy of MCDGF and pure Cu/DQ for triggering ICD was analyzed by quantifying the expression of CRT and the release of ATP and HMGB1. Compared with 1.09% of CRT exposure in the PBS group, 7.15%, 13.91%, 13.60%, and 18.72% were detected in the M-PEG + PTT, Cu/DQ, M-Cu/DQ-PEG, and MCDG + PTT group, respectively. The MCDGF + PTT treatment contributed to the highest CRT expression at 27.49% (Fig. 4e and f). Meanwhile, the ATP and HMGB1 release of each treatment group showed the same trend with CRT exposure, as shown in Fig. 4g and h. The data indicated that Cu/DQ could induce a stronger ICD than PTT, and the highest ICD efficiency occurred when combined. $Cu(DTC)_2$ was reported to induce tumor cell death by promoting the aggregation of NPL4 protein, accordingly blocking the formation of the p97-UFD1-NPL4 complex. Similarly, the expression level of NPL4 by western blot analysis revealed that the intervention of Cu/DQ and its nanoparticles was also associated with increased NPL4 levels (Fig. 4d and S13†).

2.5. *In vivo* distribution and anti-tumor activity of the nanoplatform

Photothermal imaging was then conducted *in vivo* to evaluate the photothermal conversion efficiency of MCDGF inside the

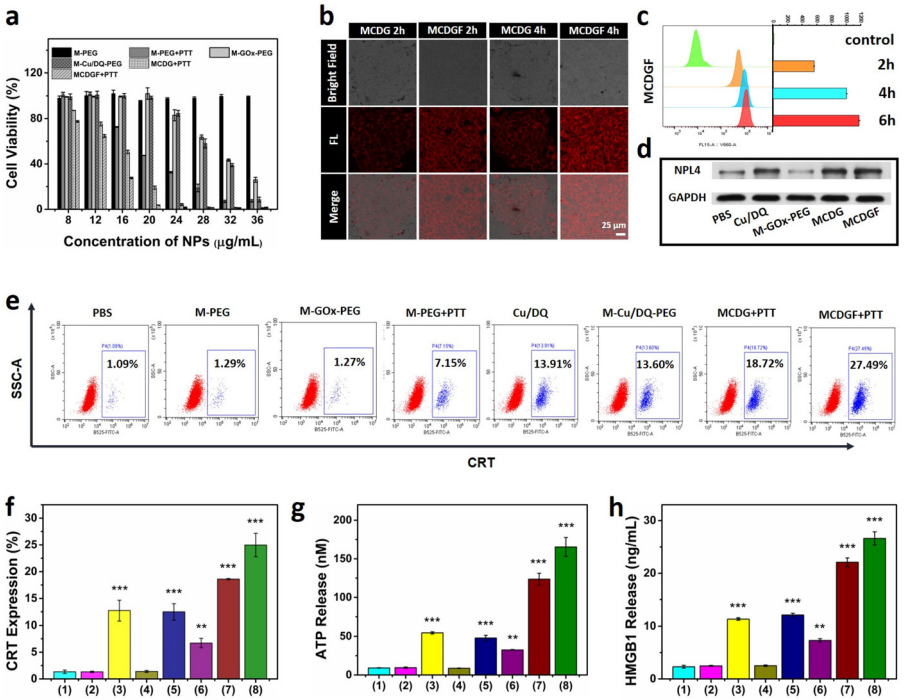

Fig. 4 (a) The viability of 4T1 cells treated with nanoparticles. (b) Confocal microscope images and (c) flow cytometric assay, with the corresponding mean fluorescence intensities (MFI) of 4T1 cells incubated with 20 μg mL^{-1} Ce6-labeled MCDGF for different periods. (d) Representative western blot images of NPL4. (e) Flow cytometric assay of calreticulin expression. (f) The analysis of calreticulin expression. The analysis of ATP release (g) and HMGB1 release (h) by enzyme-linked immunosorbent assay (ELISA). (1) PBS, (2) M-PEG, (3) Cu/DQ, (4) M-GOx-PEG, (5) M-Cu/DQ-PEG, (6) M-PEG + PTT, (7) MCDG + PTT, (8) MCDGF + PTT. Data are means ± S.D. (n = 3). *p < 0.05, **p < 0.01, and ***p < 0.001.

tumor. All animal procedures conformed to the NIH guidelines (Guide for the Care and Use of Laboratory Animals) and were approved by the ethical committee of Tongji University Animal Experiment Center (approval number was TJBB00720101).

Under irradiation for 10 min, the average local tumor temperature of the MCDG and MCDGF treated groups rapidly increased to about 42 °C and 43 °C, respectively, while a slight increase was observed in the PBS group (Fig. 5b and c), which revealed its excellent low-temperature photothermal therapeutic potential to promote the immune reactions during tumor killing. The effects of combination therapy *in vivo* were examined by administering MCDGF to 4T1-tumor-bearing mice (Fig. 5a). As shown in Fig. 5c–e, there were no significant differences between tumor growth in the PBS and M-PEG intervention groups. The growth of tumors in the Cu/DQ, M-GOx-PEG, M-Cu/DQ-PEG and M-PEG + PTT groups slowed down as compared with the rapid increase in the PBS and M-PEG groups. The above four interventions displayed mild to moderate anti-tumor activity. Importantly, both combined groups treated with MCDG + PTT and MCDGF + PTT exhibited remarkable tumor growth inhibition effects as compared with the other treatment groups (Fig. 5e and f). However, the weight gain in the MCDG + PTT group was extremely poor, indicating its obvious systemic side effects affected by the non-targeted cell-killing function. Simultaneously, the mice of the MCDGF + PTT groups displayed significant increases in body weights, indicating their promising safety profile (Fig. 5g).

Afterward, we recorded fluorescence imaging *in vivo* and *ex vivo* to assess the biodistribution of ICG-labeled MCDGF inside the tumor. Dim fluorescence was observed inside the tumor in the MCDG-ICG group with or without conjugated FA after 2 h of intravenous injection. The fluorescence signal inside the breast tumor intensified continuously over time, reaching a maximum at 12 h, especially in the tumor-targeted MCDGF-ICG group, which demonstrated the excellent tumor-targeting ability of FA. In addition, abundant signals remained in the tumor after 24 h for the ICG-labeled MCDGF group, indicating the good tumor enrichment effect of nanoparticles. Owing to the tumor-targeting effect of FA, the MCDGF nanoparticles decreased in normal tissues. With gradual dissipation over time, almost no fluorescence was observed in normal tissues such as the liver during the *ex vivo* fluorescence imaging 24 h after intravenous injection (Fig. 5h). The physiological functions of liver and kidney toxicity were also assessed. The MCDGF + PTT therapy demonstrated the most remarkable anti-tumor effect and avoided the side effects of bone marrow suppression usually accompanied by cytotoxicity, due to its FA-mediated tumor targeting ability (Fig. 5i). There was no difference in ALT and kidney function (Fig. 5j and S14†) among the groups in these experiments, and hematoxylin and eosin (H&E) staining of major organs demonstrated little damage in these tissues (Fig. S15†).

Next, we evaluated the efficiency of inducing tumor cell death *in vivo* for the different intervention groups. As shown in

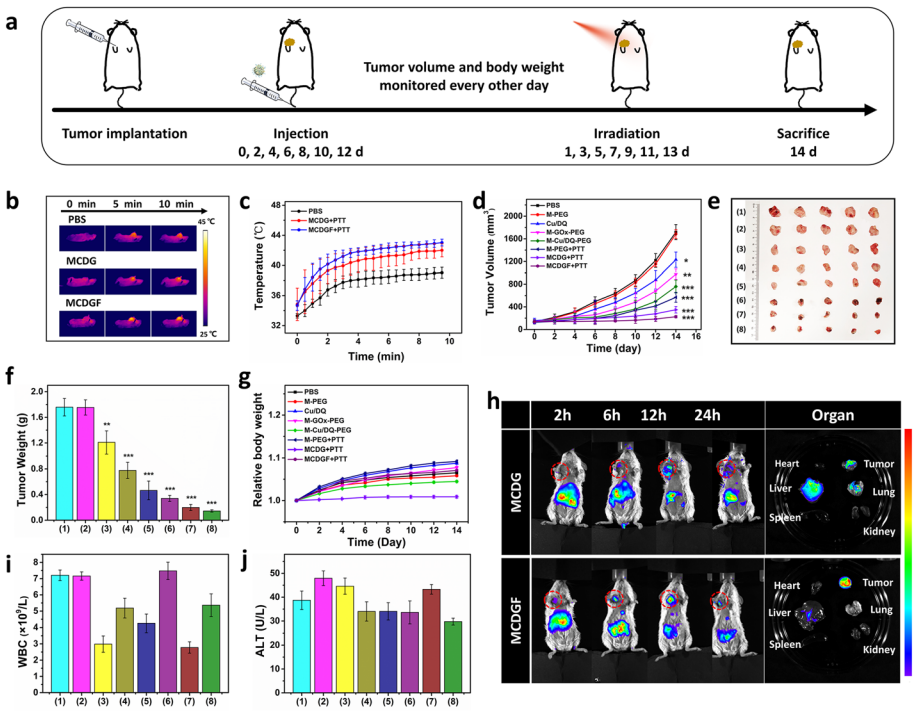

Fig. 5 (a) Schematic illustration of the tumor establishment and therapeutic outcome under 808 nm laser irradiation. (b) The thermal images of mice after intravenous injection of PBS, MCDG and MCDGF under 808 nm irradiation *in vivo*. (c) Temperature change curve of tumor sites under laser irradiation. (d) Average tumor growth curves. (e) Representative photographs and (f) tumor weights in each group obtained on day 14. (g) Relative body weight changes of mice in each treatment group. Data are means ± S.D. (n = 5). (h) Fluorescence images of BALB/c tumor-bearing mice after intravenous injection of MCDG and MCDGF at different times (2 h, 6 h, 12 h and 24 h), and *ex vivo* imaging of tumor and major organs isolated from mice at 24 h post-injection. Tumor areas in mice are circled with red dotted lines. (i and j) Physiological function assessment of bone marrow and liver toxicity in different groups. (1) PBS, (2) M-PEG, (3) Cu/DQ, (4) M-GOx-PEG, (5) M-Cu/DQ-PEG, (6) M-PEG + PTT, (7) MCDG + PTT, (8) MCDGF + PTT. *p < 0.05, **p < 0.01, and ***p < 0.001.

Fig. 6, immunohistochemical (IHC) staining for caspase 3 detected the most apoptotic cells in the MCDGF + PTT treatment group. Moreover, the simultaneously observed higher HMGB1/CRT expression indicated that MCDGF + PTT therapy was also capable of inducing the immunogenic death of tumor cells to initiate anti-tumor immunity. Given that Cu/DQ may cause cell death by inducing NPL4 aggregation, we also examined the NPL4 expression in the tumor tissues of mice in each treatment group. Mice treated with Cu/DQ or Cu/DQ-loaded nanoparticles presented with significant NPL4 in tumors.

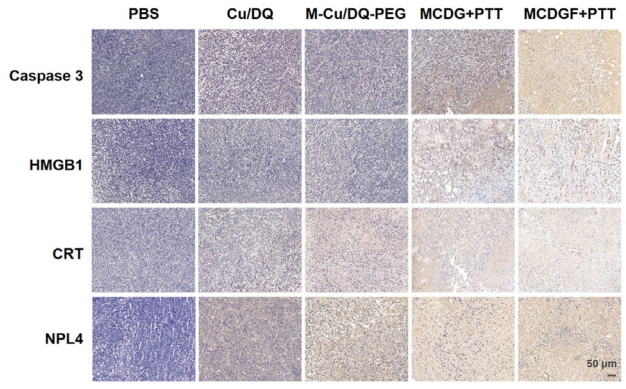

Fig. 6 Representative images of the immunohistochemistry for cell death and NPL4 in the tumors.

2.6. Assessment of *in vivo* immune responses

To further assess the *in vivo* immune responses of MCDGF + PTT intervention, the tumor mononuclear cells were collected and multicolor flow cytometry was performed. The gating strategy is shown in Fig. S16.† The pro-tumor M2 macrophages ($CD206^+$ $CD86^-$) were the dominant subtype inside the tumor in the PBS group. Impressively, after treatment with M-GOx-PEG, MCDG + PTT or MCDGF + PTT, some macrophages reverted to the anti-tumor M1 type ($CD86^+$ $CD206^-$) (Fig. 7a and b), which was consistent with the M1 macrophage polarization of H_2O_2 produced by GOx as reported previously.[31,38] The M-GOx-PEG group represented the strongest reversal effect on the M1/M2 ratio, which may be attributed to the consumption of H_2O_2 by Cu/DQ in the other two groups thereby weakening this immunological effect. The penetration of tumor-infiltrating CTLs was also observed simultaneously.

As shown in Fig. 7d and e, the CTLs ($Granzyme^+$ $CD8^+$) slightly increased to 0.25%, 0.14%, 0.43%, and 0.41% in Cu/DQ, M-PEG + PTT, MCDG and MCDG + PTT groups, respectively, with merely a 0.055% increase in the PBS group. The highest penetration rate was 0.79% in the MCDGF + PTT

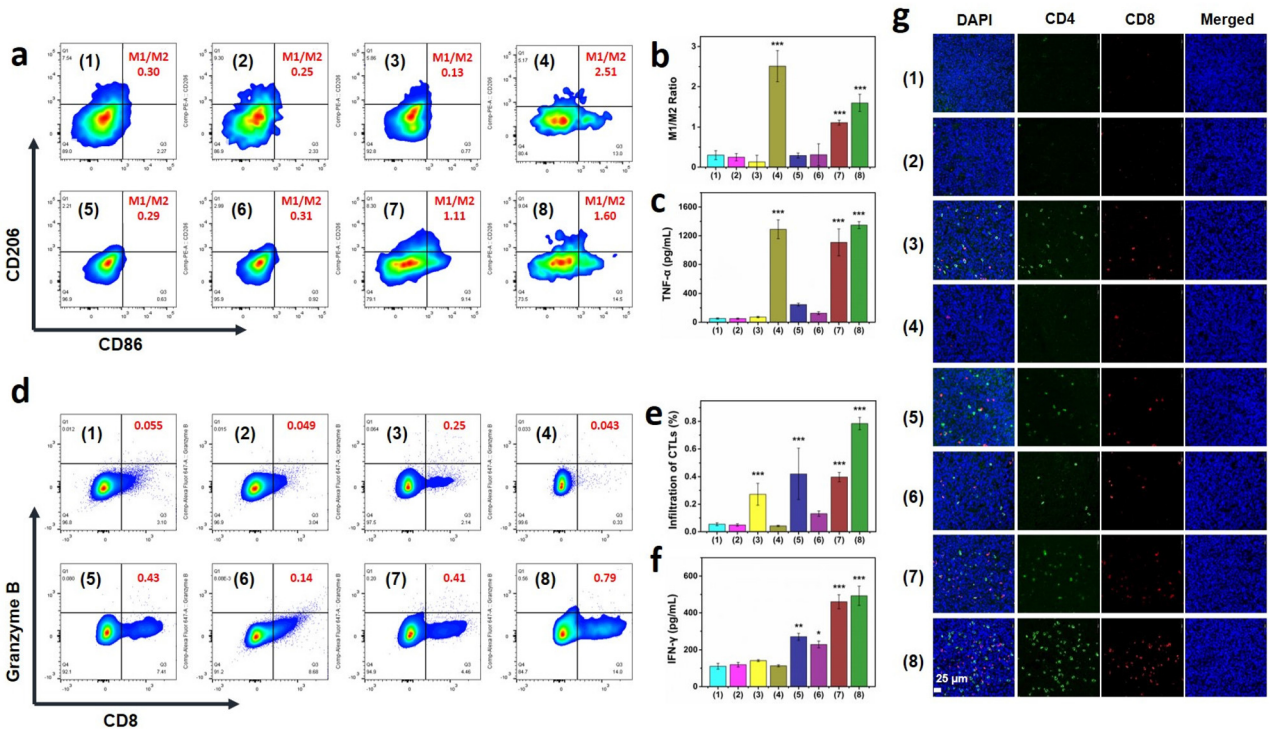

Fig. 7 (a) Representative flow cytometric analysis of macrophages, and (b) the M1/M2 ratio in different treatment groups. (c) Serum levels of TNF-α in different treatment groups of mice. (d) Representative flow cytometric analysis of tumor-infiltrating CTLs (Granzyme$^+$ CD8$^+$) and (e) percentages in different treatment groups. (f) Serum levels of IFN-γ in different treatment groups of mice. (g) Representative images of CD4$^+$ and CD8$^+$ lymphocytes in excised tumors of different treatment groups. The error bars are based on the S.D. of three mice. (1) PBS, (2) M-PEG, (3) Cu/DQ, (4) M-GOx-PEG, (5) M-Cu/DQ-PEG, (6) M-PEG + PTT, (7) MCDG + PTT, (8) MCDGF + PTT. *$p < 0.05$, **$p < 0.01$, and ***$p < 0.001$.

group, which was 14-fold that of the PBS group. These results suggest that MCDGF + PTT could significantly induce the infiltration of CTLs into the tumor. Immunofluorescence was also performed to observe the penetration of tumor-infiltrating T lymphocytes. Moreover, the elevated serum level of TNF-α and IFN-γ mainly produced by M1 macrophages and CTLs, and natural killer cells, respectively, further supported the flow cytometric analysis results (Fig. 7c and f). Compared with the PBS, M-PEG, M-GOx-PEG intervention groups, the tumor infiltration of CD4$^+$ and CD8$^+$ T cells from M-PEG + PTT, Cu/DQ, and its nanoparticle treatment groups significantly increased. Tumors from MCDGF + PTT-treated mice presented the most abundant T lymphocyte infiltration (Fig. 7g).

3. Conclusions

In conclusion, we have constructed a multifunctional nanoplatform (MCDGF) for cancer starvation therapy, PTT, chemotherapy and Cu(DTC)$_2$-enhanced immunotherapy in 4T1 cancer cell-bearing mice. Once accumulated in the tumor by active targeting, the cascade reaction between GOx and DQ was triggered. The glucose in the tumor was catalyzed into gluconic acid and H_2O_2, while DQ could be transformed into DTC by reacting with the generated H_2O_2 and chelating with co-released Cu(II) to obtain Cu(DTC)$_2$ *in situ*, producing the resultant powerful anticancer effect by starvation therapy and chemotherapy. Besides, under 808 nm laser irradiation, the anticancer activity of Cu(DTC)$_2$ was promoted by the generated hyperthermia. Most importantly, Cu(DTC)$_2$ could induce ICD, thereby enhancing the anti-tumor immune response of CTLs. Meanwhile, the H_2O_2 generated by GOx polarized TAMs toward the anti-tumor M1 phenotype to reduce the tumor burden. The above effects reshaped the tumor immune microenvironment to further eliminate cancer. Taken together, the constructed MCDGF presented a novel strategy for efficient cooperative cancer therapy by combining starvation therapy, PTT, chemotherapy, and immunotherapy, which provided a promising method for triple-negative breast cancer therapy for future clinical application translation.

Conflicts of interest

There are no conflicts to declare.

Acknowledgements

This work was supported by the National Natural Science Foundation of China (82003283, 21877084, 82073387).

References

1 H. Sung, J. Ferlay, R. L. Siegel, M. Laversanne, I. Soerjomataram, A. Jemal and F. Bray, *CA Cancer J. Clin.*, 2021, **71**, 209–249.
2 J. L. da Silva, N. C. Cardoso Nunes, P. Izetti, G. G. de Mesquita and A. C. de Melo, *Crit. Rev. Oncol. Hematol.*, 2020, **145**, 102855.
3 A. Tajbakhsh, M. Rivandi, S. Abedini, A. Pasdar and A. Sahebkar, *Crit. Rev. Oncol. Hematol.*, 2019, **140**, 17–27.
4 L. Chen, L. Zhou, C. Wang, Y. Han, Y. Lu, J. Liu, X. Hu, T. Yao, Y. Lin, S. Liang, S. Shi and C. Dong, *Adv. Mater.*, 2019, **31**, 1904997.
5 S. Pushpakom, F. Iorio, P. A. Eyers, K. J. Escott, S. Hopper, A. Wells, A. Doig, T. Guilliams, J. Latimer, C. McNamee, A. Norris, P. Sanseau, D. Cavalla and M. Pirmohamed, *Nat. Rev. Drug Discovery*, 2019, **18**, 41–58.
6 Y. Luo, X. Sun, L. Huang, J. Yan, B. Y. Yu and J. Tian, *ACS Appl. Mater. Interfaces*, 2019, **11**, 29490–29497.
7 Q. Dong, X. Wang, X. Hu, L. Xiao, L. Zhang, L. Song, M. Xu, Y. Zou, L. Chen, Z. Chen and W. Tan, *Angew. Chem., Int. Ed.*, 2018, **57**, 177–181.
8 Y. Xu, Y. Kong, J. Xu, X. Li, J. Gou, T. Yin, H. He, Y. Zhang and X. Tang, *Biomater. Sci.*, 2020, **8**, 897–911.
9 Z. Gao, Y. Li, Y. Zhang, P. An, F. Chen, J. Chen, C. You, Z. Wang and B. Sun, *Nanoscale*, 2020, **12**, 8139–8146.
10 Z. Skrott, M. Mistrik, K. K. Andersen, S. Friis, D. Majera, J. Gursky, T. Ozdian, J. Bartkova, Z. Turi, P. Moudry, M. Kraus, M. Michalova, J. Vaclavkova, P. Dzubak, I. Vrobel, P. Pouckova, J. Sedlacek, A. Miklovicova, A. Kutt, J. Li, J. Mattova, C. Driessen, Q. P. Dou, J. Olsen, M. Hajduch, B. Cvek, R. J. Deshaies and J. Bartek, *Nature*, 2017, **552**, 194–199.
11 S. Y. You, W. Rui, S. T. Chen, H. C. Chen, X. W. Liu, J. Huang and H. Y. Chen, *Biochem. Biophys. Res. Commun.*, 2019, **513**, 891–897.
12 T. Sun, W. Yang, S. M. Toprani, W. Guo, L. He, A. B. DeLeo, S. Ferrone, G. Zhang, E. Wang, Z. Lin, P. Hu and X. Wang, *Cell Commun. Signaling*, 2020, **18**, 36.
13 Y. Shao, Z. Wang, Y. Hao, X. Zhang, N. Wang, K. Chen, J. Chang, Q. Feng and Z. Zhang, *Adv. Healthcare Mater.*, 2021, **10**, 2002171.
14 L. Wang, K. Ding, C. Zheng, H. Xiao, X. Liu, L. Sun, R. Omer, Q. Feng and Z. Zhang, *Nano Lett.*, 2020, **20**, 6272–6280.
15 Q. Pan, B. Zhang, X. Peng, S. Wan, K. Luo, W. Gao, Y. Pu and B. He, *Chem. Commun.*, 2019, **55**, 13896–13899.
16 S. Bakthavatsalam, M. L. Sleeper, A. Dharani, D. J. George, T. Zhang and K. J. Franz, *Angew Chem. Int Ed*, 2018, **57**, 12780–12784.
17 X. Luo, X. Gong, L. Su, H. Lin, Z. Yang, X. Yan and J. Gao, *Angew. Chem., Int. Ed.*, 2020, **60**, 1403–1410.
18 H.-W. Liu, X.-X. Hu, K. Li, Y. Liu, Q. Rong, L. Zhu, L. Yuan, F.-L. Qu, X.-B. Zhang and W. Tan, *Chem. Sci.*, 2017, **8**, 7689–7695.
19 Z. Huang, Y. Luo, T. Zhang, Y. Ding, M. Chen, J. Chen, Q. Liu, Y. Huang and C. Zhao, *Angew. Chem., Int. Ed.*, 2022, **61**, 202203500.
20 J. Sun, K. Du, J. Diao, X. Cai, F. Feng and S. Wang, *Angew. Chem., Int. Ed.*, 2020, **59**, 12122–12128.
21 X. Li, X. Guo, J. Ling, Z. Tang, G. Huang, L. He and T. Chen, *Nanoscale*, 2021, **13**, 4705–4727.
22 X. He, Q. Wu, C. Hou, M. Hu, Q. Wang and X. Wang, *Angew. Chem., Int. Ed.*, 2023, **62**, e202218766.
23 X. Zhao, X. Li, B. Li, Y. Sun, Y. Shi, H. Shen, F. Wang, J. Li, F. Sharopov, Z. Mukhiddinov, C. Ma, K. Liu and H.-G. Hu, *Chem. Eng. J.*, 2023, **453**, 139886.
24 J. Ruan, H. Liu, B. Chen, F. Wang, W. Wang, Z. Zha, H. Qian, Z. Miao, J. Sun, T. Tian, Y. He and H. Wang, *ACS Nano*, 2021, **15**, 11428–11440.
25 J. Zhang and K. Cai, *J. Mater. Chem. B*, 2017, **5**, 8891–8903.
26 R. Li, X. Hu, F. Shang, W. Wu, H. Zhang, Y. Wang, J. Pan, S. Shi and C. Dong, *Acta Biomater.*, 2022, **148**, 218–229.
27 M. Zhang, W. Wang, F. Wu, T. Zheng, J. Ashley, M. Mohammadniaei, Q. Zhang, M. Wang, L. Li, J. Shen and Y. Sun, *Biomaterials*, 2020, **252**, 120106.
28 X. Liu, Z. Yan, Y. Zhang, Z. Liu, Y. Sun, J. Ren and X. Qu, *ACS Nano*, 2019, **13**, 5222–5230.
29 F. Zhou, J. Mei, S. Yang, X. Han, H. Li, Z. Yu, H. Qiao and T. Tang, *ACS Appl. Mater. Interfaces*, 2020, **12**, 2009–2022.
30 Z. Liu, Y. Ma, Q. Cui, J. Xu, Z. Tang, Y. Wang, C. He and X. Wang, *Biochem. Biophys. Res. Commun.*, 2020, **531**, 602–608.
31 M. Z. Zou, W. L. Liu, F. Gao, X. F. Bai, H. S. Chen, X. Zeng and X. Z. Zhang, *Adv. Mater.*, 2019, **31**, 1904495.
32 X. Hu, Y. Lu, X. Shi, T. Yao, C. Dong and S. Shi, *Chem. Commun.*, 2019, **55**, 14785–14788.
33 S. Liu, L. Wang, M. Lin, D. Wang, Z. Song, S. Li, R. Ge, X. Zhang, Y. Liu, Z. Li, H. Sun, B. Yang and H. Zhang, *ACS Appl. Mater. Interfaces*, 2017, **9**, 44293–44306.
34 X. Hu, Y. Lu, W. Zhao, M. Sun, R. Li, L. Feng, T. Yao, C. Dong and S. Shi, *Chem. Commun.*, 2021, **57**, 4158–4161.
35 Y. Zhu, N. Xin, Z. Qiao, S. Chen, L. Zeng, Y. Zhang, D. Wei, J. Sun and H. Fan, *ACS Appl. Mater. Interfaces*, 2019, **11**, 43018–43030.
36 Z. Wang, Y. Chen, H. Zhang, Y. Li, Y. Ma, J. Huang, X. Liu, F. Liu, T. Wang and X. Zhang, *Bioconjugate Chem.*, 2018, **29**, 2415–2425.
37 Z. Zhao, X. Zhang, H. Zhang, X. Shan, M. Bai, Z. Wang, F. Yang, H. Zhang, Q. Kan, B. Sun, J. Sun, Z. He and C. Luo, *Adv. Sci.*, 2021, **9**, 2104264.
38 X. Liu, P. Gao, M. Shi, Y. Chen, W. Pan, N. Li and B. Tang, *Biomater. Sci.*, 2022, **10**, 3088–3091.